

# Unsupervised Stereo via Multi-Baseline Geometry-Consistent Self-Training

Peng Xu Zhiyu Xiang\* Tingming Bai Tianyu Pu Kai Wang  
 Chaojie Ji Zhihao Yang Eryun Liu  
 College of Information Science and Electronic Engineering (ISEE)  
 Zhejiang University, China

<https://github.com/xxxupeng/S3-Stereo>

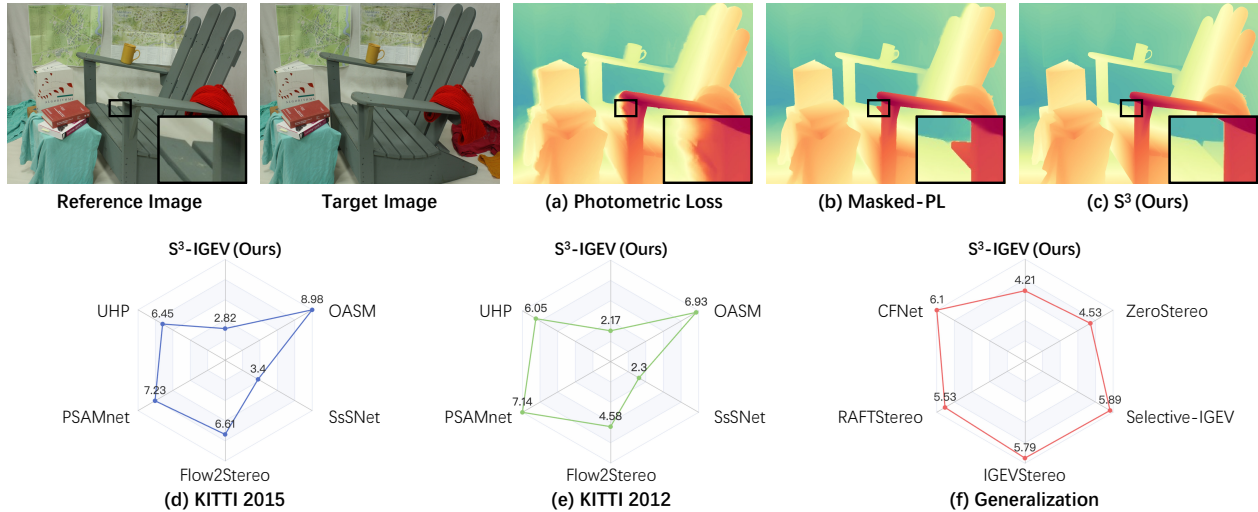


Figure 1. **Top.** Illustration of learning behaviors in occluded regions: (a) Photometric loss takes a shortcut by copying disparities from nearby visible areas; (b) Occlusion-masked photometric loss (masked-PL) fails to supervise occlusion completion, leaving these regions poorly estimated; (c) Our S<sup>3</sup> accurately predicts disparities even in heavily occluded areas. **Bottom.** S<sup>3</sup> achieves outstanding unsupervised performance on the (d) KITTI 2015 [20] and (e) KITTI 2012 [6] benchmarks, as well as zero-shot generalization in (f).

## Abstract

Photometric loss and pseudo-label-based self-training are two widely used methods for training stereo networks on unlabeled data. However, they both struggle to provide accurate supervision in occluded regions. The former lacks valid correspondences, while the latter’s pseudo labels are often unreliable. To overcome these limitations, we present S<sup>3</sup>, a simple yet effective framework based on multi-baseline geometry consistency. Unlike conventional self-training where teacher and student share identical stereo pairs, S<sup>3</sup> assigns them different target images, introducing natural visibility asymmetry. Regions occluded in the student’s view often remain visible and matchable to the teacher, enabling reliable pseudo labels even in regions where photometric supervision fails. The teacher’s disparities are rescaled to align with the student’s baseline and used to guide student learning. An occlusion-aware weighting strategy is further proposed to mitigate unreliable supervision in teacher-

occluded regions and to encourage the student to learn robust occlusion completion. To support training, we construct MBS20K, a multi-baseline stereo dataset synthesized using the CARLA simulator. Extensive experiments demonstrate that S<sup>3</sup> provides effective supervision in both occluded and non-occluded regions, achieves strong generalization performance, and surpasses previous state-of-the-art methods on the KITTI 2015 and 2012 benchmarks.

## 1. Introduction

Stereo matching aims to recover dense correspondences between rectified image pairs and plays a critical role in autonomous driving, robotics, and augmented reality. Recent unsupervised methods have achieved promising progress by leveraging photometric consistency between reference and target views [49], enabling stereo networks to learn directly from unlabeled data without ground-truth disparities.

However, photometric supervision fundamentally breaks

down in occluded regions, such as foreground–background boundaries and the non-overlapping fields of view between stereo cameras. In these areas, no valid correspondence exists in the target image, causing the photometric loss to collapse and leading networks to produce inaccurate disparity estimates, as illustrated in Fig. 1(a). To mitigate this issue, several studies [15, 34] detect occluded pixels and exclude them from photometric supervision, preventing the network from being misled during training. Although such masking strategy improves overall matching quality, Fig. 1(b) shows that training solely on visible regions remains insufficient for recovering disparities in occluded areas.

Besides photometric reconstruction, pseudo-label-based self-training provides another way to exploit unlabeled stereo pairs for unsupervised finetuning [21, 37, 46, 50]. These methods employ a teacher network to generate pseudo disparities that guide student learning. However, since the teacher and student share the same target image, regions occluded in the student’s view remain invisible to the teacher as well, making the teacher’s predictions in those areas inherently error-prone. Because self-training relies entirely on these pseudo labels, such unreliable predictions are easily propagated and reinforced by the student, ultimately limiting performance.

In this work, we explore an intuitive yet underexplored problem: must the teacher and student networks rely on the same target image in self-training? In fact, when provided with different target views, regions occluded in the student’s view often become visible to the teacher. These teacher-visible but student-occluded regions enable the teacher to generate accurate pseudo labels for supervising disparity completion. Building on this observation, we leverage multi-baseline geometry consistency to jointly enhance the matching and completion performance.

Specifically, our  $S^3$  feeds the teacher and student with the same reference image but different target images. The teacher’s disparities are rescaled to match the student’s baseline and used as pseudo labels to guide learning. To further improve occlusion completion, we introduce an occlusion-aware weighting strategy. Occlusions are first detected via thresholding on photometric consistency. We then strengthen supervision on student-occluded but teacher-visible pixels while masking those occluded in the teacher’s view, preventing unreliable pseudo labels from being propagated during training. Additionally, photometric and smoothness losses [49] are incorporated as auxiliary objectives. The photometric loss provides initial matching ability, while the teacher’s pseudo labels drive occlusion completion learning. This design allows  $S^3$  to be trained from scratch in a purely unsupervised manner, without any reliance on supervised pretraining.

To support our framework, we construct MBS20K, a multi-baseline stereo dataset synthesized using the CARLA

simulator [5]. Furthermore, to enable training on KITTI 2012 [6] and KITTI 2015 [20] datasets, we generate novel target viewpoints from the original stereo pairs. Extensive experiments validate the effectiveness of our design. As shown in Fig. 1(d)–(f),  $S^3$  achieves superior performance and strong zero-shot generalization. Our contributions are summarized as follows:

- We propose a novel asymmetric unsupervised training framework for stereo matching that leverages multi-baseline geometry consistency to enable effective supervision in occluded regions.
- We introduce an occlusion-aware weighting mechanism that emphasizes teacher-visible but student-occluded regions while masking the unreliable teacher-occluded pixels, effectively guiding the learning in both occluded and non-occluded regions.
- Our method achieves state-of-the-art results on the KITTI 2015 and KITTI 2012 benchmarks, significantly outperforming previous unsupervised methods and even surpassing several early supervised methods.
- Our method exhibits excellent generalization to diverse scenes and maintains robust performance under changing weather conditions.

## 2. Related Work

In this section, we first review the development of stereo matching, and then introduce two major paradigms for label-free stereo training.

### 2.1. Deep Stereo Matching

Over the past decades, stereo matching has undergone rapid evolution, transitioning from hand-crafted algorithms [22] to end-to-end deep learning methods [19]. Modern deep stereo networks generally follow two major architectures: 3D convolution–based cost volume regularization [3, 10, 13, 26, 27] and ConvGRU-based iterative refinement [16, 17, 47, 48]. IGEVStereo [40] employs a lightweight 3D convolutional network to provide strong initial disparity and geometric cues to the iterative units. Selective-Stereo [35] aggregates multi-frequency information to improve accuracy in edge and smooth regions. Recent works [4, 11] further enhance performance and generalization by incorporating monocular depth priors from foundation models [44].

### 2.2. Photometric-based Unsupervision

Photometric consistency has been widely used to supervise stereo networks on unlabeled data. SsSnet [49] lays the groundwork by combining photometric reconstruction with smoothness priors. Subsequent works attempt to alleviate the failure of photometric supervision in occluded regions. OASM [15] explicitly infers occlusions and masks photometrically inconsistent pixels. PASMnet [34] filters low-confidence regions by thresholding attention responses,

while UHP [45] incorporates 3D planar cues to reduce the impact of erroneous photometric guidance.

NeRFStereo [31] uses triplet inputs like ours, but its triplet photometric loss merely substitutes occluded pixels with supervision from a non-occluded pair, guiding correspondence matching rather than occlusion completion. In contrast, our method explicitly provides supervision for disparity completion.

### 2.3. Self-Training with Pseudo Labels

Self-training offers another unsupervised paradigm, in which a teacher model generates pseudo labels to train a student model. ZOLE [21] iteratively updates the network using zoomed-in patches, leveraging the extra details introduced by upsampling. DualNet [37] first trains the teacher on unlabeled data using feature-metric and data augmentation consistency losses, then freezes it to supervise the student’s disparity distribution. Inspired by [2, 9], recent works [46, 50] update the teacher via an exponential moving average (EMA) of the student’s weights. TS-PSMNet [46] introduces a confidence-based module to filter uncertain teacher predictions, while CST-Stereo [50] extracts reliable pseudo labels through multi-resolution and iterative prediction consistencies.

However, these methods face some limitations. First, they are often architecture-dependent: TS-PSMNet and DualNet are designed for 3D convolutional models, whereas CST-Stereo relies on the intermediate predictions of iterative models. Second, they still struggle to learn disparity completion due to identical occluded regions. In contrast, our method utilizes only the output disparity, making it applicable to any stereo backbone, and introduces viewpoint asymmetry to effectively supervise occluded regions. Moreover, unlike prior self-training methods that employ a well-pretrained teacher, our teacher and student can be initialized randomly and trained jointly from scratch.

## 3. Method

### 3.1. Preliminary

Given a pair of rectified stereo images, stereo matching aims to find the corresponding pixel in the target image  $I_{tgt}$  for each pixel in the reference image  $I_{ref}$ . The horizontal displacement between corresponding pixels is called disparity  $d$ . Through triangulation, the depth  $z$  of each pixel in the reference image can be calculated as:

$$z = \frac{B \cdot f}{d} \quad (1)$$

where  $B$  is the baseline length, *i.e.* the distance between the optical centers of the two cameras, and  $f$  is the focal length.

The photometric consistency assumption is commonly adopted for unsupervised stereo training [49]. The reference image  $\hat{I}_{ref}$  is reconstructed by warping the target im-

age  $I_{tgt}$  according to the predicted disparity, and the photometric difference between  $I_{ref}$  and  $\hat{I}_{ref}$  is measured as a weighted combination of SSIM [38] and  $L_1$  terms:

$$\mathcal{L}_p = \frac{\alpha}{2}(1 - \text{SSIM}(I_{ref}, \hat{I}_{ref})) + (1 - \alpha)\|I_{ref} - \hat{I}_{ref}\|_1 \quad (2)$$

In addition, smoothness loss [49] assists in encouraging smooth disparities in non-edge regions while preserving sharp transitions at edges:

$$\mathcal{L}_s = |\partial_x d|e^{-|\partial_x I_{ref}|} + |\partial_y d|e^{-|\partial_y I_{ref}|} \quad (3)$$

However, the photometric consistency assumption relies on the premise that corresponding pixels share similar appearance across views. This premise fails in occluded regions, where no valid correspondence exists, leading to erroneous supervision. Moreover, smoothness regularization alone provides only limited guidance in such challenging areas. Motivated by this limitation, we aim to provide reliable supervision in occluded regions.

### 3.2. Multi-Baseline Geometry Consistency

We design a fully unsupervised framework that exploits geometry consistency across stereo pairs with different baselines.

**Asymmetrical Input Viewpoint.** Inspired by self-training, we adopt a teacher-student architecture and intentionally introduce viewpoint asymmetry between them. Throughout the description, superscripts  $s$  and  $t$  denote the student and teacher networks, respectively.

As illustrated in Fig. 2, the student and teacher networks share the same reference image  $I_{ref}$  but receive different target views. This multi-baseline configuration leads to distinct visibility patterns: many pixels that are occluded in the student’s target view become visible in the teacher’s target view. For these student-occluded regions, the teacher can still predict accurate disparities by leveraging its strong matching capability. Given the same true depth  $z$  in the reference image, the predicted disparities  $d^s$  and  $d^t$  of the student and teacher satisfy:

$$\frac{B^s \cdot f}{d^s} = \frac{B^t \cdot f}{d^t} = z \Rightarrow d^s = r \cdot d^t, r = \frac{B^s}{B^t} \quad (4)$$

where  $B^s$  and  $B^t$  denote the baselines of the student and teacher, respectively. After rescaling the teacher’s disparity by the ratio  $r$ , the two predictions become geometrically aligned, even though they observe the scene under different baselines.

**Robust Student and Momentum Teacher.** We apply data augmentation only to the student’s input images, including color jittering and random occlusion. This asymmetric design imposes a more challenging optimization objective, compelling the student network to learn stronger and more robust feature representations for accurate disparity prediction [43].

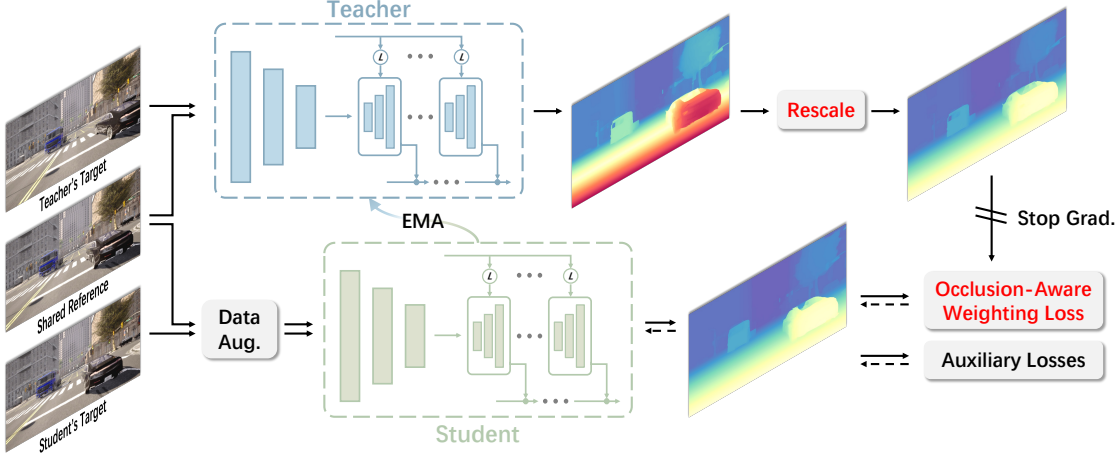


Figure 2. **Overview of  $S^3$ .** Stereo pairs sharing the same reference view but different target views are fed into the teacher and student, respectively. This asymmetric configuration allows the teacher to observe regions that are occluded in the student’s view. The teacher’s disparities are rescaled to align with the student’s baseline and used to supervise the student through geometry-consistent loss with occlusion-aware weighting. Data augmentation is applied to the student to encourage robust feature learning. The teacher is updated via exponential moving average (EMA) of the student’s weights with gradients stopped.

The student network is randomly initialized, and the teacher is initialized with the same weights and updated using an exponential moving average (EMA) of the student’s weights. Formally, the update rule is  $\theta^t \leftarrow m \cdot \theta^t + (1 - m) \cdot \theta^s$ , where  $\theta^s$  and  $\theta^t$  denote the student and teacher weights, and  $m$  is a momentum parameter following a cosine schedule as in BYOL [9]. In our experiments, the momentum teacher further improves performance over the fixed teacher. During inference, only the teacher network is used for disparity estimation.

**Geometry-Consistent Loss.** The core supervision signal of our framework is the geometry-consistency loss, which enforces the student prediction to align with the rescaled teacher disparity:

$$\mathcal{L}_g = \|d^s - r \cdot d^t\|_1 \quad (5)$$

This loss provides effective guidance for both non-occluded and occluded regions, since the teacher can observe areas that are invisible in the student’s target view.

### 3.3. Occlusion-Aware Weighting

Given that the teacher and student observe different target views, each reference image can be divided into three regions: (1) non-occluded to both networks, (2) occluded to the teacher, and (3) occluded to the student but visible to the teacher. In region (2), the teacher’s predictions are unreliable and may mislead the student. In contrast, in region (3), the student cannot estimate accurate disparities from photometric prior alone, whereas the teacher’s predictions remain trustworthy. Moreover, we observe that occluded regions are much harder to learn. Applying the same penalty to both occluded and non-occluded areas is insufficient to

improve performance in occluded regions.

To address these issues, we introduce an occlusion-aware weight map  $\mathcal{A}$  that suppresses unreliable supervision in region (2) and strengthens learning in region (3). Since occluded pixels naturally incur higher photometric errors, we first compute the teacher’s photometric loss  $\mathcal{L}_p^t$  and apply a threshold  $\tau$  to remove teacher-occluded pixels. We further employ the auto-masking strategy [8] to eliminate pixels with high uncertainty. Combining these two filtering strategies yields a binary mask  $\mathcal{M}^t$  for the teacher; the same process is used to obtain  $\mathcal{M}^s$  for the student. The occlusion-aware weight map  $\mathcal{A}$  is then defined per pixel as:

$$\mathcal{A} = \begin{cases} 1, & \mathcal{M}^t = \text{True}, \mathcal{M}^s = \text{True} \\ 0, & \mathcal{M}^t = \text{False} \\ \omega, & \mathcal{M}^t = \text{True}, \mathcal{M}^s = \text{False} \end{cases} \quad (6)$$

where  $\omega > 1$ . Applying this weight map to the geometry-consistent loss  $\mathcal{L}_g$  ensures reliable supervision for the student and enhances its learning in occluded regions. Examples of the resulting weight maps are visualized in Fig. 3.

### 3.4. Final Loss

Teacher-student frameworks often suffer from collapsing to trivial solutions [9]. In our case, both teacher and student could take a shortcut by predicting constant zero disparities, which would make  $\mathcal{L}_g$  vanish. To prevent this degeneration, we incorporate photometric loss  $\mathcal{L}_p$  and smoothness loss  $\mathcal{L}_s$  (defined in Eq. (2) and Eq. (3)) as auxiliary objectives to regularize the student’s learning.

The final loss is formulated as:

$$\mathcal{L} = \mathcal{L}_g \odot \mathcal{A} + \lambda_p \mathcal{L}_p \odot \mathcal{M}^s + \lambda_s \mathcal{L}_s \quad (7)$$

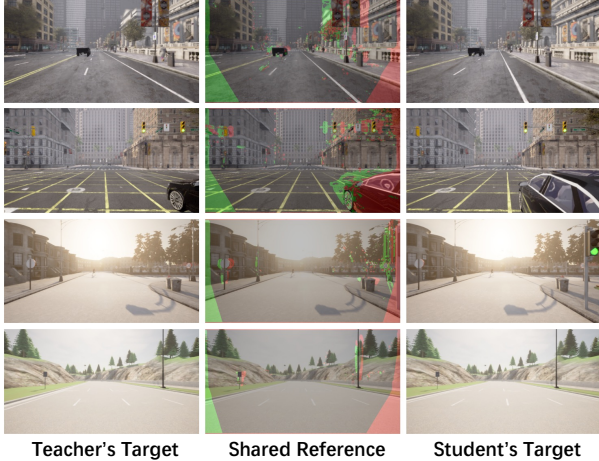


Figure 3. **Visualization of the occlusion-aware weight map.** Red areas indicate regions occluded in the teacher’s target view, while green areas correspond to regions occluded in the student’s target view but visible in the teacher’s view. The remaining regions are visible in both views.

where  $\odot$  denotes element-wise multiplication. Following [8], we set  $\alpha = 0.85$  in Eq. (2) and  $\lambda_s = 0.001\lambda_p$ .

### 3.5. Synthetic Multi-Baseline Data

To support the training of our framework, we synthesize a multi-baseline stereo dataset using the CARLA simulator [5]. At each timestamp, five horizontally aligned RGB cameras capture images with a uniform baseline of 0.5 m between adjacent cameras. Each image has a focal length of 480 px and a resolution of  $540 \times 960$  px. In total, we collect 20,417 multi-baseline samples.

**Triplet Sampling Strategy.** During training, we randomly select one image as the reference and choose two others from the remaining four as target views, forming a triplet input. Unlike the conventional stereo setup, we do not restrict the target view to be on the right side of the reference. If the selected target lies on the left, we horizontally flip both images before feeding them into the network and flip the predicted disparity back afterward.

## 4. Experiments

### 4.1. Evaluation Datasets and Protocols

We evaluate our framework on five public real-world datasets: KITTI 2012 [6], KITTI 2015 [20], Middlebury(H) [23], ETH3D [24], and DrivingStereo [42].

For KITTI 2012 and 2015, we submit the test set predictions to the official benchmarks for fair comparison with other methods. We further evaluate zero-shot generalization by directly testing the model trained on synthetic data on the training sets of KITTI, Middlebury, and ETH3D. These datasets provide occlusion masks, enabling quantitative ver-

ification of our improvement in occluded regions. In addition, we evaluate robustness under challenging weather conditions on DrivingStereo.

**Evaluation Metrics.** We employ three standard metrics: EPE, Out-x, and D1. EPE measures the mean absolute disparity error over valid pixels. Out-x denotes the percentage of pixels whose absolute error exceeds x pixels. D1 counts pixels for which both the absolute error exceeds 3 px and the relative error exceeds 5%. Following common practice, we report Out-3 on KITTI and DrivingStereo, Out-2 on Middlebury, and Out-1 on ETH3D.

### 4.2. Implementation Details

We adopt IGEVStereo [40] as our primary backbone owing to its strong accuracy and generalization capability. To verify the effectiveness and generality of our framework, we further conduct experiments on GwcNet [10], CFNet [26], RAFTStereo [17], and MonSter [4]. For unsupervised pre-training, we train on the proposed MBS20K dataset for 200K iterations with a batch size of 16. We use the Adam optimizer [14] with a one-cycle learning rate schedule [28], where the maximum learning rate is set to  $2e-4$ . For unsupervised finetuning on the KITTI 2012 [6] and KITTI 2015 [20] training sets, we additionally generate novel viewpoints to match the input configuration required by our framework (details are provided in the supplementary material). The model is trained for 50K iterations on the augmented multi-baseline KITTI data, with the maximum learning rate reduced to  $5e-5$ . Images are randomly cropped to  $384 \times 512$  during pretraining and  $256 \times 512$  during finetuning. All experiments are conducted on four NVIDIA RTX 4090 GPUs. The hyperparameters are set to  $\lambda_p = 10$ ,  $\tau = 0.1$ , and  $\omega = 2$ , selected via grid search.

### 4.3. Comparisons with State-of-the-art

We conduct a fair comparison against state-of-the-art methods on the KITTI 2012 [6] and 2015 [20] benchmarks. Following prior works, the evaluation is conducted under two settings: (1) fully unsupervised, where neither pretraining nor finetuning uses any ground-truth disparities; and (2) unsupervised finetuning, where pretraining may use ground-truth disparity but finetuning is performed without ground-truth supervision.

In the fully unsupervised setting, where the model is pretrained on MBS20K and finetuned on KITTI without ground truth, S<sup>3</sup>-IGEVStereo achieves a new state-of-the-art performance on both KITTI 2015 and 2012, as shown in Tab. 1 (third block). It surpasses prior methods such as Reversing-PSM [1] and SsSnet [49], even though SsSnet leverages the large-scale KITTI raw dataset [7]. Compared with SsSnet, S<sup>3</sup>-IGEVStereo improves the main benchmark metrics on KITTI 2015 and 2012 by 17.06% and 5.65%, respectively. Remarkably, it attains comparable or even superior accuracy

| Method                           | KITTI 2015         |             |             |                   |             |             | KITTI 2012 |             |             |            |             |             |
|----------------------------------|--------------------|-------------|-------------|-------------------|-------------|-------------|------------|-------------|-------------|------------|-------------|-------------|
|                                  | NOC                |             |             | ALL               |             |             | NOC        |             |             | ALL        |             |             |
|                                  | D1-BG              | D1-FG       | D1-ALL      | D1-BG             | D1-FG       | D1-ALL      | EPE        | Out-2       | Out-3       | EPE        | Out-2       | Out-3       |
|                                  | Pretraining w/ GT  |             |             | Finetuning w/ GT  |             |             |            |             |             |            |             |             |
| DispNet [19]                     | 4.11               | 3.72        | 4.05        | 4.32              | 4.41        | 4.34        | 0.9        | 7.38        | 4.11        | 1.0        | 8.11        | 4.65        |
| SGM-Net [25]                     | 2.23               | 7.44        | 3.09        | 2.66              | 8.64        | 3.66        | 0.7        | 3.60        | 2.29        | 0.9        | 5.15        | 3.50        |
| GCNet [13]                       | 2.02               | 5.58        | 2.61        | 2.21              | 6.16        | 2.87        | 0.6        | 2.71        | 1.77        | 0.7        | 3.46        | 2.30        |
| AAANet [41]                      | 1.80               | 4.93        | 2.32        | 1.99              | 5.39        | 2.55        | 0.5        | 2.90        | 1.91        | 0.6        | 3.60        | 2.42        |
|                                  | Pretraining w/ GT  |             |             | Finetuning w/o GT |             |             |            |             |             |            |             |             |
| MADNet [30]                      | 3.45               | 8.41        | 4.27        | 3.75              | 9.20        | 4.66        | —          | —           | —           | —          | —           | —           |
| AdaStereo [29]                   | 2.39               | 5.06        | 2.83        | 2.59              | 5.55        | 3.08        | —          | —           | —           | —          | —           | —           |
| DualNet [37]                     | 2.28               | 4.66        | 2.67        | 2.46              | 5.25        | 2.92        | 0.6        | —           | 2.06        | 0.6        | —           | 2.59        |
| <b>S<sup>3</sup>-IGEV (Ours)</b> | <b>2.06</b>        | <b>4.43</b> | <b>2.45</b> | <b>2.21</b>       | <b>4.86</b> | <b>2.65</b> | <b>0.5</b> | <b>3.11</b> | <b>1.92</b> | <b>0.6</b> | <b>3.69</b> | <b>2.31</b> |
|                                  | Pretraining w/o GT |             |             | Finetuning w/o GT |             |             |            |             |             |            |             |             |
| MC-CNN-WS [32]                   | 3.06               | 9.42        | 4.11        | 3.78              | 10.93       | 4.97        | 0.8        | 4.76        | 3.02        | 1.0        | 6.57        | 4.45        |
| SsNet [49]                       | 2.46               | 6.13        | 3.06        | 2.70              | 6.92        | 3.40        | 0.7        | 3.34        | 2.30        | 0.8        | 4.24        | 3.00        |
| OASM [15]                        | 5.44               | 17.30       | 7.39        | 6.89              | 19.42       | 8.98        | 1.3        | 9.01        | 6.39        | 2.0        | 11.17       | 8.60        |
| Flow2Stereo [18]                 | 4.77               | 14.03       | 6.29        | 5.01              | 14.62       | 6.61        | 1.0        | 6.56        | 4.58        | 1.1        | 7.32        | 5.11        |
| Reversing-PSM [1]                | 2.97               | 8.33        | 3.86        | 3.13              | 8.70        | 4.06        | —          | —           | —           | —          | —           | —           |
| PASMnet [34]                     | 5.02               | 15.16       | 6.69        | 5.41              | 16.36       | 7.23        | 1.3        | —           | 7.14        | 1.5        | —           | 8.57        |
| EMR-MSF [12]                     | 8.30               | 14.16       | 9.27        | 8.61              | 15.15       | 9.70        | —          | —           | —           | —          | —           | —           |
| UHP [45]                         | 4.65               | 12.37       | 5.93        | 5.00              | 13.70       | 6.45        | 1.2        | 9.08        | 6.05        | 1.3        | 10.37       | 7.09        |
| <b>S<sup>3</sup>-IGEV (Ours)</b> | <b>2.25</b>        | <b>4.30</b> | <b>2.59</b> | <b>2.44</b>       | <b>4.75</b> | <b>2.82</b> | <b>0.6</b> | <b>3.54</b> | <b>2.17</b> | <b>0.6</b> | <b>4.21</b> | <b>2.60</b> |

Table 1. **Quantitative results on the KITTI 2015 and 2012 benchmarks.** NOC denotes evaluation in non-occluded regions, while ALL includes all pixels. KITTI 2015 additionally reports foreground (FG) and background (BG) performance. S<sup>3</sup>-IGEV achieves strong performance in both the fully unsupervised (third block) and unsupervised finetuning (second block) settings. It is comparable to or even surpasses GCNet [13], the pioneering work of 3D convolution-based stereo matching.

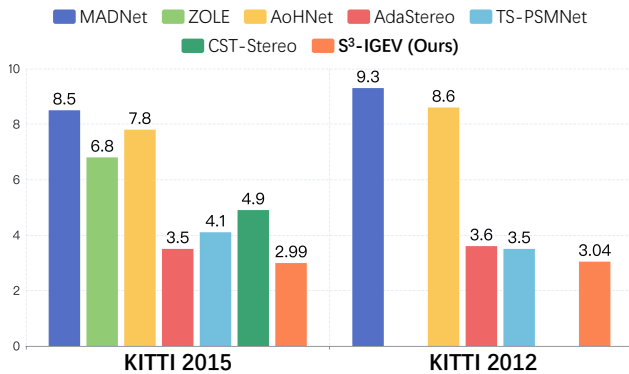


Figure 4. **Quantitative comparison** on the KITTI training sets [6, 20]. The D1 error over all valid pixels is reported. ZOLE [21] and CST-Stereo [50] do not provide results on KITTI 2012.

to early supervised models such as DispNet [19] and GCNet [13]. To the best of our knowledge, S<sup>3</sup>-IGEV is the first fully unsupervised model that surpasses GCNet, the pioneering work of 3D convolution-based stereo matching, on the KITTI 2015 benchmark. These results highlight the effectiveness of our multi-baseline geometry consistency in providing reliable supervision on unlabeled data.

In the unsupervised finetuning setting, S<sup>3</sup>-IGEV is initialized with the official pretrained weights on Scene-

Flow [19]. As shown in Tab. 1 (second block), it further improves over the fully unsupervised version. Compared with the photometric-based method [29, 30] and the self-training method [37], S<sup>3</sup>-IGEV consistently achieves much lower error across all metrics. We also evaluate on the KITTI training sets following [21, 33], and the results in Fig. 4 show that S<sup>3</sup>-IGEV achieves the lowest D1 errors on both KITTI 2012 and 2015, outperforming recent self-training methods such as TS-PSMNet [46] and CST-Stereo [50]. These gains primarily stem from the viewpoint asymmetry, which allows the teacher to observe regions occluded in the student’s view and provide reliable pseudo labels for occlusion completion.

Overall, S<sup>3</sup> unifies photometric- and pseudo-label-based unsupervision within a single framework, demonstrating strong performance in both fully unsupervised training and unsupervised finetuning. It enables high-quality stereo learning on real-world data without any ground-truth annotations.

#### 4.4. Zero-Shot Generalization

Zero-shot generalization is essential for ensuring the reliability and safety of stereo-based systems deployed in unseen environments. In this section, we evaluate the generalization ability of S<sup>3</sup> across diverse scenes and weather conditions.

| Method  | KITTI 2015  |             | KITTI 2012   |             | Middlebury   |             | ETH3D       |             | DrivingStereo |             |             |             |
|---|-------------|-------------|--------------|-------------|--------------|-------------|-------------|-------------|---------------|-------------|-------------|-------------|
|   | OCC         | ALL         | OCC          | ALL         | OCC          | ALL         | OCC         | ALL         | Sunny         | Cloudy      | Rainy       | Foggy       |
| PSMNet [3]                                      | 47.64       | 28.42       | 63.20        | 27.32       | 62.30        | 34.51       | 28.56       | 15.39       | 40.14         | 43.95       | 56.19       | 69.69       |
| GwcNet [10]                                     | 29.07       | 12.53       | 45.65        | 12.67       | 47.13        | 24.11       | 21.37       | 11.09       | 17.12         | 25.56       | 28.19       | 29.23       |
| CFNet [26]                                      | 16.42       | 6.10        | 30.25        | 5.15        | 44.55        | 20.22       | 11.89       | 5.87        | 4.70          | 5.30        | 12.48       | 5.54        |
| RAFTStereo [17]                                 | 12.70       | 5.53        | 28.35        | 4.84        | 28.00        | 11.96       | 6.02        | 3.04        | 4.23          | 4.19        | 12.77       | 3.09        |
| IGEVStereo [40]                                 | 14.26       | 5.79        | 33.66        | 5.59        | 24.28        | 9.91        | 9.76        | 4.39        | 4.59          | 5.15        | 15.47       | 4.49        |
| NeRFStereo-RAFT <sup>†</sup> [31]               | 14.62       | 5.43        | 26.97        | 4.04        | 31.10        | 10.38       | 8.35        | 3.07        | 2.88          | 2.91        | 10.20       | 3.93        |
| Selective-IGEV [35]                             | 13.82       | 5.89        | 31.85        | 5.68        | 22.59        | 9.17        | 9.81        | 4.43        | 5.05          | 5.24        | 13.51       | 4.10        |
| DEFOMStereo <sup>‡</sup> [39]                   | 12.57       | 4.99        | 21.95        | 4.21        | 20.64        | <b>6.91</b> | 5.14        | 2.24        | 3.61          | 3.75        | 13.53       | 2.88        |
| MonSter <sup>‡</sup> [4]                        | <u>9.64</u> | <u>3.45</u> | <u>18.82</u> | <u>3.37</u> | <u>18.42</u> | 7.70        | <u>3.53</u> | <u>1.45</u> | 3.48          | 3.17        | 5.27        | 5.03        |
| ZeroStereo <sup>†</sup> [36]                    | 10.53       | 4.53        | 19.41        | 3.50        | 21.27        | 7.40        | 6.25        | 2.19        | 2.59          | 2.36        | 13.07       | <u>1.89</u> |
| <b>S<sup>3</sup>-IGEV (Ours)</b>                | 10.37       | 4.21        | 21.49        | 3.48        | 23.46        | 8.94        | 7.98        | 2.76        | <u>2.15</u>   | <u>1.87</u> | <u>5.07</u> | <b>1.64</b> |
| <b>S<sup>3</sup>-MonSter<sup>‡</sup> (Ours)</b> | <b>8.17</b> | <b>2.68</b> | <b>17.26</b> | <b>2.48</b> | <b>17.78</b> | <u>7.13</u> | <b>3.47</b> | <b>1.35</b> | <b>1.91</b>   | <b>1.78</b> | <b>2.35</b> | 2.11        |

Table 2. **Zero-shot generalization across diverse scenes and weathers.** We report outlier metrics (Out-x) in occluded (OCC) and all (ALL) regions for the real-world datasets [6, 20, 23, 24]. All methods are re-evaluated using their officially released weights to ensure fair comparison. <sup>†</sup>Real data is used during training. <sup>‡</sup>Foundation model-based methods.

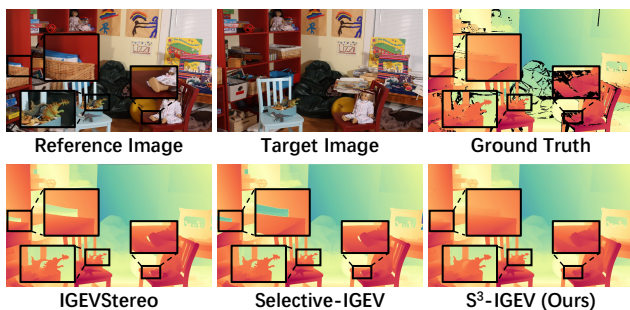


Figure 5. **Qualitative comparison of the occluded areas** between IGEVStereo [40], Selective-IGEV [35], and our S<sup>3</sup>-IGEV. Please zoom in for more details.

**Cross-Scene Evaluation.** As shown in Tab. 2, S<sup>3</sup>-IGEV demonstrates strong generalization across both indoor and outdoor datasets [6, 20, 23, 24]. Compared with the baseline IGEVStereo [40], S<sup>3</sup>-IGEV consistently improves performance in occluded regions, reducing outlier rates on KITTI 2015, KITTI 2012, Middlebury, and ETH3D by 27.28%, 36.16%, 3.38%, and 18.24%, respectively. Quantitative results in Fig. 5 further confirm these gains. Both IGEVStereo [40] and Selective-IGEV [35] apply uniform penalties to occluded and non-occluded pixels, which often leads to erroneous disparity estimates in occluded regions. In contrast, S<sup>3</sup>-IGEV substantially improves disparity completion in these challenging areas, benefiting from the proposed occlusion-aware weighting strategy.

We further compare with NeRFStereo [31]. Although NeRFStereo also adopts triplet inputs, its triplet photometric loss mainly aims to reduce photometric noise in occlusions, thus improving matching rather than disparity completion. This is reflected in the occlusion metrics across four datasets: NeRFStereo-RAFT exhibits mixed behavior

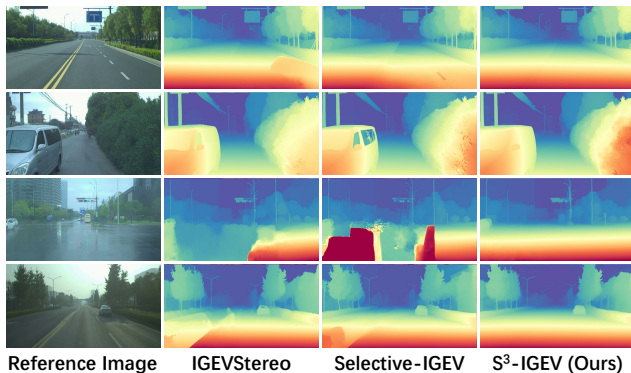


Figure 6. **Qualitative comparison under different weathers** between IGEVStereo [40], Selective-IGEV [35], and our S<sup>3</sup>-IGEV. From top to bottom: sunny, cloudy, rainy, and foggy.

compared to the original RAFTStereo [17], improving some metrics while degrading others. By contrast, our S<sup>3</sup>-IGEV surpasses NeRFStereo on both occlusion and overall metrics, demonstrating that our viewpoint-asymmetric geometry consistency provides more effective triplet-based supervision for both matching and completion.

Recent foundation model-based methods [4, 11] have shown excellent zero-shot generalization. Building upon these advances, applying S<sup>3</sup> to MonSter [4] further enhances its generalization performance.

**Cross-Weather Evaluation.** We further evaluate under diverse weather conditions using the DrivingStereo dataset [42], which contains four subsets: sunny, cloudy, rainy, and foggy. As shown in Tab. 2, S<sup>3</sup>-IGEV achieves superior cross-weather robustness, significantly reducing outlier rates across all conditions compared with the baseline [40]. In particular, under rainy conditions, most existing methods suffer from severe performance degradation,

|            | $\mathcal{L}_g$ | $\mathcal{L}_p$ | $\mathcal{L}_s$ | OCC          | NOC         | ALL         |
|------------|-----------------|-----------------|-----------------|--------------|-------------|-------------|
| (A)        |                 | ✓               | ✓               | 97.44        | 5.51        | 7.14        |
| (B)        | ✓               | ✓               |                 | <u>10.62</u> | 4.49        | <u>4.64</u> |
| (C)        | ✓               |                 | ✓               | 11.23        | 5.14        | 5.29        |
| <b>(D)</b> | ✓               | ✓               | ✓               | <b>10.37</b> | <b>4.05</b> | <b>4.21</b> |
| (D)*       | ✓               | ✓               | ✓               | 10.87        | 4.98        | 5.12        |

Table 3. **Ablation study of loss terms** in Eq. (7). \*EMA is not used to update the teacher network.

| PTF | AMF | OAE | OCC          | NOC         | ALL         |
|-----|-----|-----|--------------|-------------|-------------|
|     |     |     | 13.67        | 4.93        | 5.13        |
| ✓   |     |     | 13.49        | 4.76        | 4.96        |
|     | ✓   |     | 13.27        | 4.43        | 4.64        |
| ✓   | ✓   |     | <u>12.39</u> | 4.06        | <u>4.25</u> |
| ✓   | ✓   | ✓   | <b>10.37</b> | <b>4.05</b> | <b>4.21</b> |

Table 4. **Ablation study of the filtering and enhancement strategies.** PTF: photometric threshold filtering. AMF: auto-masking filtering. OAE: occlusion-aware enhancement.

posing safety risks for real-world stereo systems. In contrast,  $S^3$ -IGEVStereo maintains reliable accuracy with only 5.07% outliers. Qualitative examples in Fig. 6 further demonstrate our improvement. Both IGEVStereo [40] and Selective-IGEVStereo [35] struggle on water-logged road surfaces, whereas  $S^3$ -IGEVStereo produces accurate and stable disparity estimates.

#### 4.5. Ablation Study

We conduct comprehensive ablation experiments to analyze the contributions of each key component in  $S^3$ . All variants are trained on the proposed MBS20K dataset, and zero-shot generalization is evaluated on the KITTI 2015 training set [20] using the Out-3 metric over occluded (OCC), non-occluded (NOC), and all (ALL) regions.

**Loss Terms.** As shown in Tab. 3, conventional unsupervised losses (A) fail to provide effective supervision in occluded regions, resulting in almost completely erroneous predictions. This limitation stems from the inherent inability of photometric supervision to provide reliable learning signals in occluded regions. By introducing the geometry-consistency loss  $\mathcal{L}_g$ ,  $S^3$  provides valid supervision in both occluded and non-occluded regions, yielding large accuracy gains across all metrics. When combined with photometric and smoothness regularization (D), the full loss achieves the best overall performance, confirming that these objectives are complementary in improving matching and completion.

**Momentum Teacher.** In Tab. 3, we further prove the benefit of the momentum teacher. Compared to the fixed teacher (D)\*, the momentum teacher (D) offers more stable and generalizable supervision, leading to consistent improvements in all regions.

**Occlusion-Aware Weighting.** We further ablate the components used to construct the occlusion-aware weight

| Method                                | OCC          | NOC         | ALL         |
|---------------------------------------|--------------|-------------|-------------|
| GwcNet [10]                           | 29.07        | 12.17       | 12.53       |
| <b><math>S^3</math>-GwcNet (Ours)</b> | <b>12.70</b> | <b>4.46</b> | <b>4.65</b> |
| CFNet [26]                            | 16.42        | 5.87        | 6.10        |
| <b><math>S^3</math>-CFNet (Ours)</b>  | <b>11.88</b> | <b>4.26</b> | <b>4.44</b> |
| RAFTStereo [17]                       | 12.70        | 5.34        | 5.53        |
| <b><math>S^3</math>-RAFT (Ours)</b>   | <b>11.73</b> | <b>3.92</b> | <b>4.09</b> |

Table 5. **Generality of our framework.** We additionally conduct experiments on the 3D convolution-based backbones [10, 26] and the iteration-based backbone [17].

map, as shown in Tab. 4. The auto-masking strategy [8] improves performance by removing pixels with high photometric uncertainty (*i.e.*, weakly textured or infinite-depth areas). Building upon this, photometric threshold filtering further excludes teacher-occluded pixels, refining the supervision signal and improving overall accuracy. Finally, our occlusion-aware enhancement strategy imposes stronger supervision on student-occluded but teacher-visible regions, achieving the lowest errors and confirming the benefit of targeted learning for occlusion completion.

**Generality.** Since  $S^3$  directly supervises the output disparity predictions, it is compatible with various stereo architectures. We evaluate the generality on both the 3D convolution-based backbones [10, 26] and the iteration-based backbone [17]. As shown in Tab. 5,  $S^3$  consistently improves performance. Even on RAFTStereo [17], which already performs well in occluded regions,  $S^3$  further reduces the occlusion error from 12.70% to 11.73%, demonstrating its strong generality and effectiveness across architectures.

## 5. Conclusion

In this paper, we present  $S^3$ , a fully unsupervised stereo framework built upon multi-baseline geometry consistency. By assigning different target viewpoints to the teacher and student,  $S^3$  exploits natural visibility asymmetry to provide reliable supervision across both occluded and non-occluded regions. An occlusion-aware weighting mechanism further emphasizes teacher-visible but student-occluded areas, enabling effective learning of disparity completion where photometric cues fail. Comprehensive experiments demonstrate that  $S^3$  achieves state-of-the-art unsupervised performance on the KITTI 2012 and 2015 benchmarks, and exhibits strong generalization across diverse scenes and robustness under challenging weather conditions.

**Discussion.** While  $S^3$  demonstrates strong performance, its current fine-tuning relies on augmented KITTI data, where the generated images may contain unrealistic regions that limit learning. Future work will focus on collecting real multi-baseline stereo data to validate our framework.

## References

- [1] Filippo Aleotti, Fabio Tosi, Li Zhang, Matteo Poggi, and Stefano Mattoccia. Reversing the cycle: self-supervised deep stereo through enhanced monocular distillation. In *European Conference on Computer Vision*, pages 614–632. Springer, 2020. 5, 6, 3
- [2] Mathilde Caron, Hugo Touvron, Ishan Misra, Hervé Jégou, Julien Mairal, Piotr Bojanowski, and Armand Joulin. Emerging properties in self-supervised vision transformers. In *Proceedings of the IEEE/CVF international conference on computer vision*, pages 9650–9660, 2021. 3
- [3] Jia-Ren Chang and Yong-Sheng Chen. Pyramid stereo matching network. In *Proceedings of the IEEE conference on computer vision and pattern recognition*, pages 5410–5418, 2018. 2, 7, 3
- [4] Junda Cheng, Longliang Liu, Gangwei Xu, Xianqi Wang, Zhaoxing Zhang, Yong Deng, Jinliang Zang, Yurui Chen, Zhipeng Cai, and Xin Yang. Monster: Marry monodepth to stereo unleashes power. *arXiv preprint arXiv:2501.08643*, 2025. 2, 5, 7, 1, 3
- [5] Alexey Dosovitskiy, German Ros, Felipe Codevilla, Antonio Lopez, and Vladlen Koltun. Carla: An open urban driving simulator. In *Conference on robot learning*, pages 1–16. PMLR, 2017. 2, 5, 1
- [6] Andreas Geiger, Philip Lenz, and Raquel Urtasun. Are we ready for autonomous driving? the kitti vision benchmark suite. In *2012 IEEE conference on computer vision and pattern recognition*, pages 3354–3361. IEEE, 2012. 1, 2, 5, 6, 7, 3
- [7] Andreas Geiger, Philip Lenz, Christoph Stiller, and Raquel Urtasun. Vision meets robotics: The kitti dataset. *International Journal of Robotics Research (IJRR)*, 2013. 5
- [8] Clément Godard, Oisín Mac Aodha, Michael Firman, and Gabriel J Brostow. Digging into self-supervised monocular depth estimation. In *Proceedings of the IEEE/CVF international conference on computer vision*, pages 3828–3838, 2019. 4, 5, 8, 1, 2
- [9] Jean-Bastien Grill, Florian Strub, Florent Altché, Corentin Tallec, Pierre Richemond, Elena Buchatskaya, Carl Doersch, Bernardo Avila Pires, Zhaohan Guo, Mohammad Gheshlaghi Azar, et al. Bootstrap your own latent—a new approach to self-supervised learning. *Advances in neural information processing systems*, 33:21271–21284, 2020. 3, 4
- [10] Xiaoyang Guo, Kai Yang, Wukui Yang, Xiaogang Wang, and Hongsheng Li. Group-wise correlation stereo network. In *Proceedings of the IEEE/CVF Conference on Computer Vision and Pattern Recognition*, pages 3273–3282, 2019. 2, 5, 7, 8, 3
- [11] Hualie Jiang, Zhiqiang Lou, Laiyan Ding, Rui Xu, Minglang Tan, Wenjie Jiang, and Rui Huang. Defom-stereo: Depth foundation model based stereo matching. *arXiv preprint arXiv:2501.09466*, 2025. 2, 7, 3
- [12] Zijie Jiang and Masatoshi Okutomi. Emr-msf: Self-supervised recurrent monocular scene flow exploiting ego-motion rigidity. In *Proceedings of the IEEE/CVF International Conference on Computer Vision*, pages 69–78, 2023. 6, 3
- [13] Alex Kendall, Hayk Martirosyan, Saumitro Dasgupta, Peter Henry, Ryan Kennedy, Abraham Bachrach, and Adam Bry. End-to-end learning of geometry and context for deep stereo regression. In *Proceedings of the IEEE international conference on computer vision*, pages 66–75, 2017. 2, 6
- [14] Diederik P. Kingma and Jimmy Ba. Adam: A method for stochastic optimization, 2017. 5
- [15] Ang Li and Zejian Yuan. Occlusion aware stereo matching via cooperative unsupervised learning. In *Asian Conference on Computer Vision*, pages 197–213. Springer, 2018. 2, 6, 3
- [16] Jiankun Li, Peisen Wang, Pengfei Xiong, Tao Cai, Ziwei Yan, Lei Yang, Jiangyu Liu, Haoqiang Fan, and Shuaicheng Liu. Practical stereo matching via cascaded recurrent network with adaptive correlation. In *Proceedings of the IEEE/CVF Conference on Computer Vision and Pattern Recognition*, pages 16263–16272, 2022. 2
- [17] Lahav Lipson, Zachary Teed, and Jia Deng. Raft-stereo: Multilevel recurrent field transforms for stereo matching. In *2021 International Conference on 3D Vision (3DV)*, pages 218–227. IEEE, 2021. 2, 5, 7, 8, 3
- [18] Pengpeng Liu, Irwin King, Michael R Lyu, and Jia Xu. Flow2stereo: Effective self-supervised learning of optical flow and stereo matching. In *Proceedings of the IEEE/CVF conference on computer vision and pattern recognition*, pages 6648–6657, 2020. 6, 3
- [19] Nikolaus Mayer, Eddy Ilg, Philip Hausser, Philipp Fischer, Daniel Cremers, Alexey Dosovitskiy, and Thomas Brox. A large dataset to train convolutional networks for disparity, optical flow, and scene flow estimation. In *Proceedings of the IEEE conference on computer vision and pattern recognition*, pages 4040–4048, 2016. 2, 6
- [20] Moritz Menze and Andreas Geiger. Object scene flow for autonomous vehicles. In *Proceedings of the IEEE conference on computer vision and pattern recognition*, pages 3061–3070, 2015. 1, 2, 5, 6, 7, 8, 3, 4
- [21] Jiahao Pang, Wenxiu Sun, Chengxi Yang, Jimmy Ren, Ruichao Xiao, Jin Zeng, and Liang Lin. Zoom and learn: Generalizing deep stereo matching to novel domains. In *Proceedings of the IEEE Conference on Computer Vision and Pattern Recognition*, pages 2070–2079, 2018. 2, 3, 6
- [22] Daniel Scharstein and Richard Szeliski. A taxonomy and evaluation of dense two-frame stereo correspondence algorithms. *International journal of computer vision*, 47(1):7–42, 2002. 2
- [23] Daniel Scharstein, Heiko Hirschmüller, York Kitajima, Greg Krathwohl, Nera Nešić, Xi Wang, and Porter Westling. High-resolution stereo datasets with subpixel-accurate ground truth. In *German conference on pattern recognition*, pages 31–42. Springer, 2014. 5, 7, 3
- [24] Thomas Schops, Johannes L Schonberger, Silvano Galliani, Torsten Sattler, Konrad Schindler, Marc Pollefeys, and Andreas Geiger. A multi-view stereo benchmark with high-resolution images and multi-camera videos. In *Proceedings of the IEEE Conference on Computer Vision and Pattern Recognition*, pages 3260–3269, 2017. 5, 7, 3
- [25] Akihito Seki and Marc Pollefeys. Sgm-nets: Semi-global matching with neural networks. In *Proceedings of the*

- IEEE conference on computer vision and pattern recognition*, pages 231–240, 2017. 6
- [26] Zhelun Shen, Yuchao Dai, and Zhibo Rao. Cfnnet: Cascade and fused cost volume for robust stereo matching. In *Proceedings of the IEEE/CVF Conference on Computer Vision and Pattern Recognition*, pages 13906–13915, 2021. 2, 5, 7, 8, 3
- [27] Z. Shen, Y. Dai, et al. Pcw-net: Pyramid combination and warping cost volume for stereo matching. In *ECCV*, 2022. 2
- [28] Leslie N. Smith. A disciplined approach to neural network hyper-parameters: Part 1 – learning rate, batch size, momentum, and weight decay, 2018. 5
- [29] Xiao Song, Guorun Yang, Xinge Zhu, Hui Zhou, Zhe Wang, and Jianping Shi. Adastereo: a simple and efficient approach for adaptive stereo matching. In *Proceedings of the IEEE/CVF Conference on Computer Vision and Pattern Recognition*, pages 10328–10337, 2021. 6, 3
- [30] Alessio Tonioni, Fabio Tosi, Matteo Poggi, Stefano Mattoccia, and Luigi Di Stefano. Real-time self-adaptive deep stereo. In *Proceedings of the IEEE/CVF Conference on Computer Vision and Pattern Recognition*, pages 195–204, 2019. 6, 3
- [31] Fabio Tosi, Alessio Tonioni, Daniele De Gregorio, and Matteo Poggi. Nerf-supervised deep stereo. In *Proceedings of the IEEE/CVF conference on computer vision and pattern recognition*, pages 855–866, 2023. 3, 7
- [32] Stepan Tulyakov, Anton Ivanov, and Francois Fleuret. Weakly supervised learning of deep metrics for stereo reconstruction. In *Proceedings of the IEEE International Conference on Computer Vision*, pages 1339–1348, 2017. 6, 3
- [33] Haiyang Wang, Xinchao Wang, Jie Song, Jie Lei, and Mingli Song. Faster self-adaptive deep stereo. In *Proceedings of the Asian Conference on Computer Vision*, 2020. 6
- [34] Longguang Wang, Yulan Guo, Yingqian Wang, Zhengfa Liang, Zaiping Lin, Jungang Yang, and Wei An. Parallax attention for unsupervised stereo correspondence learning. *IEEE Transactions on Pattern Analysis and Machine Intelligence*, 44(4):2108–2125, 2022. 2, 6, 3
- [35] Xianqi Wang, Gangwei Xu, Hao Jia, and Xin Yang. Selective-stereo: Adaptive frequency information selection for stereo matching. In *Proceedings of the IEEE/CVF Conference on Computer Vision and Pattern Recognition*, pages 19701–19710, 2024. 2, 7, 8, 3
- [36] Xianqi Wang, Hao Yang, Gangwei Xu, Junda Cheng, Min Lin, Yong Deng, Jinliang Zang, Yurui Chen, and Xin Yang. Zerostereo: Zero-shot stereo matching from single images. *arXiv preprint arXiv:2501.08654*, 2025. 7, 1, 3
- [37] Yun Wang, Jiahao Zheng, Chenghao Zhang, Zhanjie Zhang, Kunhong Li, Yongjian Zhang, and Junjie Hu. Dualnet: Robust self-supervised stereo matching with pseudo-label supervision. In *Proceedings of the AAAI Conference on Artificial Intelligence*, pages 8178–8186, 2025. 2, 3, 6
- [38] Zhou Wang, Alan C Bovik, Hamid R Sheikh, and Eero P Simoncelli. Image quality assessment: from error visibility to structural similarity. *IEEE transactions on image processing*, 13(4):600–612, 2004. 3
- [39] Bowen Wen, Matthew Trepte, Joseph Aribido, Jan Kautz, Orazio Gallo, and Stan Birchfield. Foundationstereo: Zero-shot stereo matching. *arXiv preprint arXiv:2501.09898*, 2025. 7
- [40] Gangwei Xu, Xianqi Wang, Xiaohuan Ding, and Xin Yang. Iterative geometry encoding volume for stereo matching. In *Proceedings of the IEEE/CVF Conference on Computer Vision and Pattern Recognition*, pages 21919–21928, 2023. 2, 5, 7, 8, 3
- [41] Haofei Xu and Juyong Zhang. Aanet: Adaptive aggregation network for efficient stereo matching. In *Proceedings of the IEEE/CVF Conference on Computer Vision and Pattern Recognition*, pages 1959–1968, 2020. 6
- [42] Guorun Yang, Xiao Song, Chaoqin Huang, Zhidong Deng, Jianping Shi, and Bolei Zhou. Drivingstereo: A large-scale dataset for stereo matching in autonomous driving scenarios. In *Proceedings of the IEEE/CVF conference on computer vision and pattern recognition*, pages 899–908, 2019. 5, 7
- [43] Lihe Yang, Bingyi Kang, Zilong Huang, Xiaogang Xu, Jiashi Feng, and Hengshuang Zhao. Depth anything: Unleashing the power of large-scale unlabeled data. In *Proceedings of the IEEE/CVF Conference on Computer Vision and Pattern Recognition*, pages 10371–10381, 2024. 3
- [44] Lihe Yang, Bingyi Kang, Zilong Huang, Zhen Zhao, Xiaogang Xu, Jiashi Feng, and Hengshuang Zhao. Depth anything v2. *Advances in Neural Information Processing Systems*, 37:21875–21911, 2024. 2
- [45] Ruizhi Yang, Xingqiang Li, Rigang Cong, and Jinsong Du. Unsupervised hierarchical iterative tile refinement network with 3d planar segmentation loss. *IEEE Robotics and Automation Letters*, 9(3):2678–2685, 2024. 3, 6
- [46] Xin Yue, Zongqing Lu, Xiangru Lin, Wenjia Ren, Zhijing Shao, Haonan Hu, Yu Zhang, and Qingmin Liao. Semistereo: A universal stereo matching framework for imperfect data via semi-supervised learning. In *Proceedings of the IEEE/CVF Conference on Computer Vision and Pattern Recognition*, pages 646–655, 2024. 2, 3, 6
- [47] Haoliang Zhao, Huizhou Zhou, Yongjun Zhang, Yong Zhao, Yitong Yang, and Ting Ouyang. Eai-stereo: Error aware iterative network for stereo matching. In *Proceedings of the Asian Conference on Computer Vision*, pages 315–332, 2022. 2
- [48] Haoliang Zhao, Huizhou Zhou, Yongjun Zhang, Jie Chen, Yitong Yang, and Yong Zhao. High-frequency stereo matching network. In *Proceedings of the IEEE/CVF Conference on Computer Vision and Pattern Recognition*, pages 1327–1336, 2023. 2
- [49] Yiran Zhong, Yuchao Dai, and Hongdong Li. Self-supervised learning for stereo matching with self-improving ability. *arXiv preprint arXiv:1709.00930*, 2017. 1, 2, 3, 5, 6
- [50] Jingyi Zhou, Peng Ye, Haoyu Zhang, Jiakang Yuan, Rao Qiang, Liu YangChenXu, Wu Cailin, Feng Xu, and Tao Chen. Consistency-aware self-training for iterative-based stereo matching. In *Proceedings of the Computer Vision and Pattern Recognition Conference*, pages 16641–16650, 2025. 2, 3, 6

# Unsupervised Stereo via Multi-Baseline Geometry-Consistent Self-Training

## Supplementary Material

### A. MBS20K Dataset

**Data Collection Setup.** We deploy a Tesla Model 3 within the CARLA simulator [5], equipped with five synchronized RGB cameras, to conduct autonomous driving across seven towns (01, 02, 03, 05, 06, 07, and 10). Driving trajectories are first recorded under clear weather at noon, and then replayed under additional weather conditions (clear, cloudy, rainy) and lighting conditions (noon, sunset, night) to enrich diversity.

The vehicle travels at speeds up to 30 km/h, and frames are captured at 0.5-second intervals. All five cameras are mounted rigidly at a height of 2.26 meters above ground, with a uniform baseline of 0.5 meters between adjacent cameras.

**Additional Ground-Truth Depth.** Although our method does not require ground-truth depth for training, we additionally collect metric depth to facilitate broader use of our dataset. Specifically, we attach a depth camera co-located with the leftmost RGB camera and record its output during data collection. This enables researchers to explore fully supervised stereo matching, depth estimation, multi-task learning, or evaluation protocols that rely on accurate depth measurements.

Following the official CARLA configuration [5], depth maps are encoded as three-channel RGB images. The metric depth  $z$  (in meters) can be decoded from the RGB channels using:

$$z = 1000 \times \frac{R + G \times 256 + B \times 256^2}{256^3 - 1}. \quad (8)$$

**Dataset Statistics.** Tab. 6 summarizes the total number of multi-baseline image sets collected in each town under different combinations of weather and illumination. Representative examples from seven towns are shown in Figs. 10 to 16, illustrating the diversity of environments and lighting conditions available in the dataset.

**Input Triplet Sampling Strategy.** Given a set of  $N$  simultaneously captured images, we construct training triplets using the following procedure:

1. Randomly select one image as the reference view;
2. Independently sample two target views (with replacement) from the remaining  $(N - 1)$  images to serve as the student and teacher target inputs.

This sampling protocol yields a total of  $N(N - 1)^2$  distinct triplets per timestamp. Under our configuration with  $N = 5$  cameras, this produces  $5 \times 4^2 = 80$  unique triplets at each timestamp. Scaling across our entire dataset produces a total of 1,633,360 ( $20, 417 \times 80$ ) training triples.

### B. Occlusion-Aware Weight Map

Fig. 7 illustrates the three types of visibility regions that arise under our multi-baseline configuration. To clearly expose these asymmetric visibility patterns, we visualize cases in which the teacher’s and student’s target views are positioned on opposite sides of the shared reference image. Red regions mark pixels occluded in the teacher’s target view and are therefore down-weighted to prevent harmful supervision. Green regions represent pixels occluded in the student’s view but visible to the teacher. These pixels receive stronger supervision to encourage the student to learn disparity completion. Remaining areas are visible in both views. For clarity, we disable auto-masking [8] in these visualizations.

### C. Novel View Extrapolation

KITTI 2015 [20] and 2012 [6] only provide binocular stereo pairs, which are insufficient for the multi-baseline configuration required by our training framework. To address this limitation, we generate additional left-extrapolated and right-extrapolated views from each stereo pair using a two-stage pipeline that combines disparity-based warping with generative inpainting.

As illustrated in Fig. 8, we first deploy MonSter [4] to estimate the left and right disparity maps. Using these predicted disparities, we warp the left image further to the left and the right image further to the right, producing two novel views. Since the warping is performed using disparities estimated under the original stereo baseline, the relative camera displacement between each extrapolated view and its neighboring raw image remains consistent with the baseline of the input stereo pair.

Disparity estimation is not perfect, especially around depth discontinuities, where the network often over-smooths boundaries and produces bleeding artifacts. These artifacts propagate into the warped views, causing inaccurate or distorted content in occluded regions. To mitigate this issue, we dilate the occlusion mask before inpainting to ensure that the problematic pixels are removed. We then apply the inpainting model [36] to synthesize visually plausible content in these masked regions. This generative inpainting step restores structure and texture in occluded areas, making the extrapolated views significantly more reliable for training.

The final output consists of four images per timestamp: the original stereo pair and the two extrapolated views (in-painted further left and in-painted further right images). As with our MBS20K dataset, we then sample training triplets

| #Set    | Clear Night | Clear Noon | Clear Sunset | Cloudy Noon | Rainy Noon | All   |
|---------|-------------|------------|--------------|-------------|------------|-------|
| Town 01 | 630         | 630        | 629          | 632         | 631        | 3152  |
| Town 02 | 424         | 424        | 424          | 425         | 424        | 2121  |
| Town 03 | 647         | 649        | 648          | 649         | 648        | 3241  |
| Town 05 | 563         | 563        | 567          | 567         | 564        | 2824  |
| Town 06 | 820         | 821        | 820          | 821         | 821        | 4103  |
| Town 07 | 442         | 440        | 441          | 440         | 440        | 2203  |
| Town 10 | 552         | 557        | 554          | 554         | 556        | 2773  |
| All     | 4078        | 4084       | 4083         | 4088        | 4084       | 20417 |

Table 6. **Statistics of our MBS20K dataset** collected in the CARLA simulator [5]. Each set contains five color images and one depth image.



Figure 7. **Visualization of our occlusion-aware weight map.** Red areas indicate regions occluded in the teacher’s target view, while green areas correspond to regions occluded in the student’s target view but visible in the teacher’s view. The remaining regions are visible in both views. To more clearly show the differences in occluded regions between the teacher and student networks, the auto-masking strategy [8] is not used here.

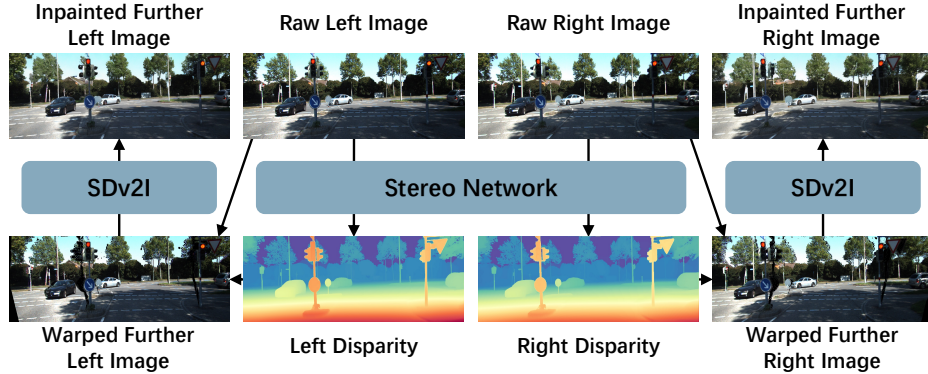


Figure 8. **Multi-baseline data generation pipeline** from stereo image pair. SDv2I: Stable Diffusion v2 Inpainting model [36].

| Method  | KITTI 2015  |              |             |             |              |             | KITTI 2012 |             |             |            |             |             |
|---|-------------|--------------|-------------|-------------|--------------|-------------|------------|-------------|-------------|------------|-------------|-------------|
|   | NOC         |              |             | ALL         |              |             | NOC        |             |             | ALL        |             |             |
|   | D1-BG       | D1-FG        | D1-ALL      | D1-BG       | D1-FG        | D1-ALL      | EPE        | Out-2       | Out-3       | EPE        | Out-2       | Out-3       |
| MADNet [30]                                   | 3.45        | 8.41         | 4.27        | 3.75        | 9.20         | 4.66        | —          | —           | —           | —          | —           | —           |
| AdaStereo [29]                                | 2.39        | 5.06         | 2.83        | 2.59        | 5.55         | 3.08        | —          | —           | —           | —          | —           | —           |
| DualNet [37]                                  | 2.28        | 4.66         | 2.67        | 2.46        | 5.25         | 2.92        | 0.6        | —           | 2.06        | 0.6        | —           | 2.59        |
| MC-CNN-WS [32]                                | 3.06        | 9.42         | 4.11        | 3.78        | 10.93        | 4.97        | 0.8        | 4.76        | 3.02        | 1.0        | 6.57        | 4.45        |
| SsSnet [49]                                   | 2.46        | 6.13         | 3.06        | 2.70        | 6.92         | 3.40        | 0.7        | 3.34        | 2.30        | 0.8        | 4.24        | 3.00        |
| OASM [15]                                     | 5.44        | 17.30        | 7.39        | 6.89        | 19.42        | 8.98        | 1.3        | 9.01        | 6.39        | 2.0        | 11.17       | 8.60        |
| Flow2Stereo [18]                              | 4.77        | 14.03        | 6.29        | 5.01        | 14.62        | 6.61        | 1.0        | 6.56        | 4.58        | 1.1        | 7.32        | 5.11        |
| Reversing-PSM [1]                             | 2.97        | 8.33         | 3.86        | 3.13        | 8.70         | 4.06        | —          | —           | —           | —          | —           | —           |
| PASMnet [34]                                  | 5.02        | 15.16        | 6.69        | 5.41        | 16.36        | 7.23        | 1.3        | —           | 7.14        | 1.5        | —           | 8.57        |
| EMR-MSF [12]                                  | 8.30        | 14.16        | 9.27        | 8.61        | 15.15        | 9.70        | —          | —           | —           | —          | —           | —           |
| UHP [45]                                      | 4.65        | 12.37        | 5.93        | 5.00        | 13.70        | 6.45        | 1.2        | 9.08        | 6.05        | 1.3        | 10.37       | 7.09        |
| <b>S<sup>3</sup>-IGEVS<sup>‡</sup> (Ours)</b> | <b>2.67</b> | <b>12.36</b> | <b>4.27</b> | <b>2.89</b> | <b>13.19</b> | <b>4.60</b> | <b>0.7</b> | <b>4.18</b> | <b>2.72</b> | <b>0.8</b> | <b>5.05</b> | <b>3.27</b> |

Table 7. **KITTI benchmark results.** <sup>‡</sup>No KITTI data is used during training. NOC denotes evaluation in non-occluded regions, while ALL includes all pixels. KITTI 2015 additionally reports foreground (FG) and background (BG) performance.

from these four images for use in our S<sup>3</sup> framework.

## D. More Results

**Zero-Shot Generalization on KITTI Benchmark.** We additionally test the zero-shot generalization performance of S<sup>3</sup>-IGEVS on the official KITTI benchmarks [6, 20]. Tab. 7 shows that although S<sup>3</sup>-IGEVS is trained only on synthetic data, it still surpasses several unsupervised methods trained directly on KITTI. This strong zero-shot performance demonstrates that our method successfully guides the network to develop strong stereo matching capability, enabling it to generalize robustly to real-world scenes without domain-specific finetuning.

**Performance in Non-Occluded Regions.** Tab. 8 supplements Tab. 2 in the main paper by reporting the performance of all methods in non-occluded (NOC) regions of KITTI 2015 [20], KITTI 2012 [6], Middlebury [23], and ETH3D [24] datasets. Compared with its baseline IGEVStereo [40], S<sup>3</sup>-IGEVS achieves consistent gains across all four datasets. Our S<sup>3</sup>-MonSter further improves

| Method  | KT15        | KT12        | MB          | ETH3D       |
|---|-------------|-------------|-------------|-------------|
| PSMNet [3]                                      | 28.13       | 26.50       | 30.18       | 14.74       |
| GwcNet [10]                                     | 12.17       | 11.91       | 20.41       | 10.49       |
| CFNet [26]                                      | 5.87        | 4.58        | 16.33       | 5.57        |
| RAFTStereo [17]                                 | 5.34        | 4.29        | 9.06        | 2.85        |
| IGEVStereo [40]                                 | 5.60        | 4.92        | 7.25        | 4.06        |
| NeRFStereo-RAFT <sup>†</sup> [31]               | 5.23        | 3.51        | 6.79        | 2.78        |
| Selective-IGEVS [35]                            | 5.70        | 5.06        | 6.79        | 2.78        |
| DEFOMStereo <sup>‡</sup> [11]                   | 4.79        | 3.83        | <b>4.39</b> | 2.08        |
| MonSter <sup>‡</sup> [4]                        | <u>3.30</u> | <u>3.03</u> | 5.86        | <u>1.32</u> |
| ZeroStereo <sup>†</sup> [36]                    | 4.36        | 3.16        | <u>4.90</u> | 1.93        |
| <b>S<sup>3</sup>-IGEVS (Ours)</b>               | 4.05        | 3.08        | 6.34        | 2.51        |
| <b>S<sup>3</sup>-MonSter<sup>‡</sup> (Ours)</b> | <b>2.53</b> | <b>2.16</b> | 5.59        | <b>1.19</b> |

Table 8. **Performance in non-occluded (NOC) regions** across four datasets [6, 20, 23, 24]. <sup>†</sup>Real data is used during training. <sup>‡</sup>Foundation model-based methods.

upon MonSter [4] and reaches new state-of-the-art results on three datasets. Taken together with Tab. 2, these results confirm that the proposed geometry-consistent training framework enhances disparity prediction in both occluded

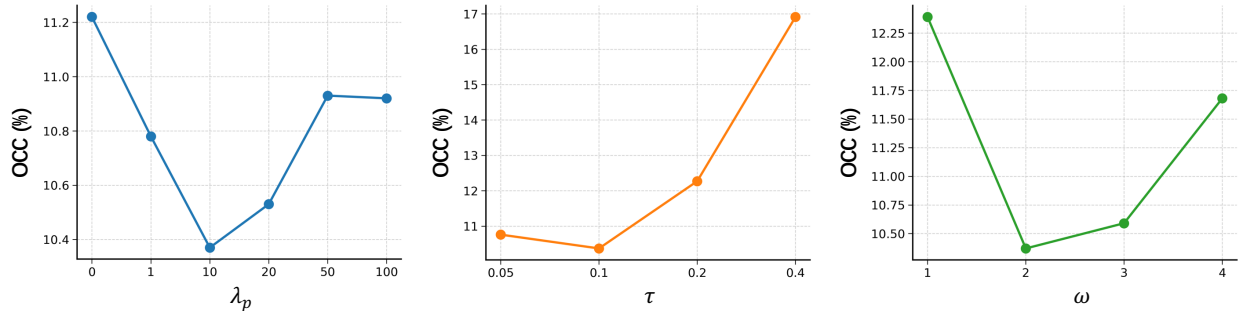


Figure 9. **Ablation study of the hyperparameters.** We report Out-3 error in occluded regions of the KITTI 2015 training set [20].

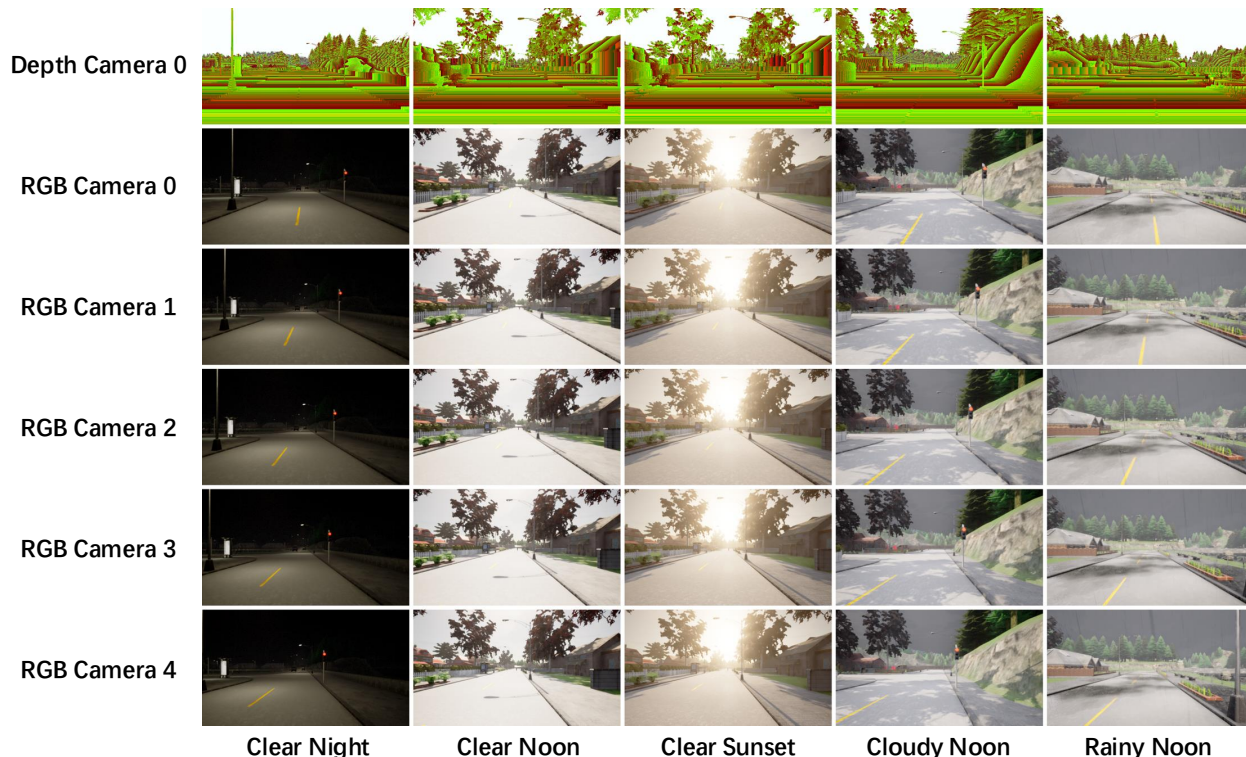


Figure 10. **Examples** of our synthetic data in **Town 01**.

and non-occluded regions.

### E. Hyperparameter Search

We conduct ablations to determine the optimal hyperparameters. As shown in Fig. 9, incorporating the photometric loss improves performance, but too large  $\lambda_p$  introduces noise because the occlusion masks are not perfect. Similarly, a loose threshold  $\tau$  fails to sufficiently filter out occluded pixels and rapidly degrades performance. For  $\omega$ , the moderate value helps the network learn disparity completion in occluded regions. However, since these regions are both sparse and highly challenging, overly strong supervi-

sion can force the network to overfit noisy pseudo labels, harming convergence and leading to worse performance. Overall, setting  $\lambda_p = 10$ ,  $\tau = 0.1$ , and  $\omega = 2$  achieves the best occlusion outlier rate on the KITTI 2015 training set [20].

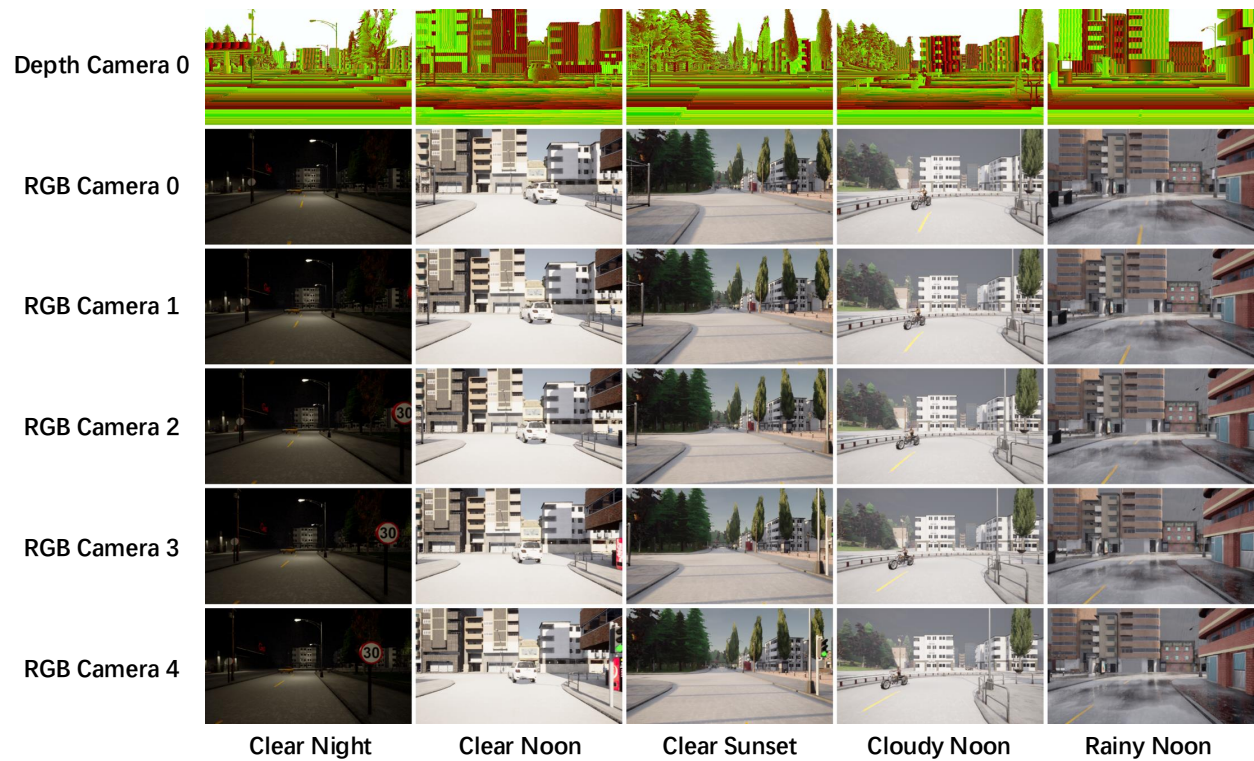


Figure 11. **Examples** of our synthetic data in **Town 02**.

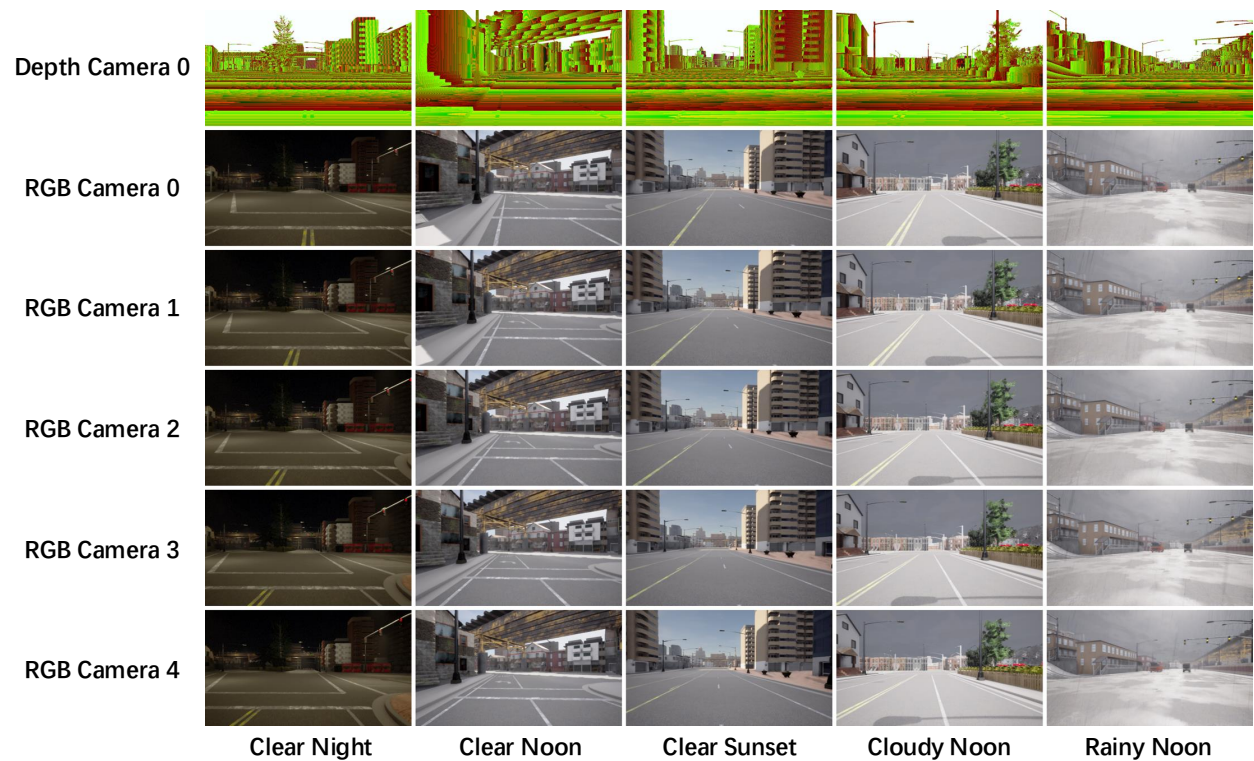


Figure 12. **Examples** of our synthetic data in **Town 03**.

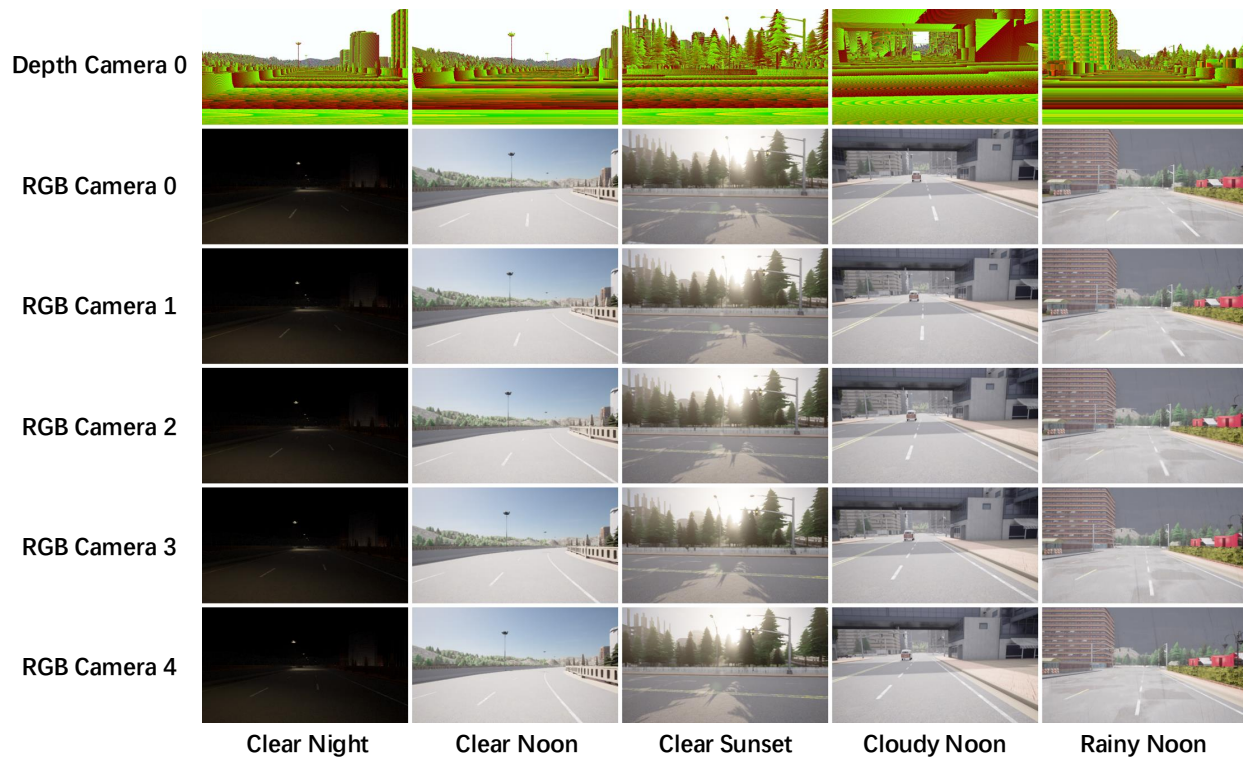


Figure 13. **Examples** of our synthetic data in **Town 05**.

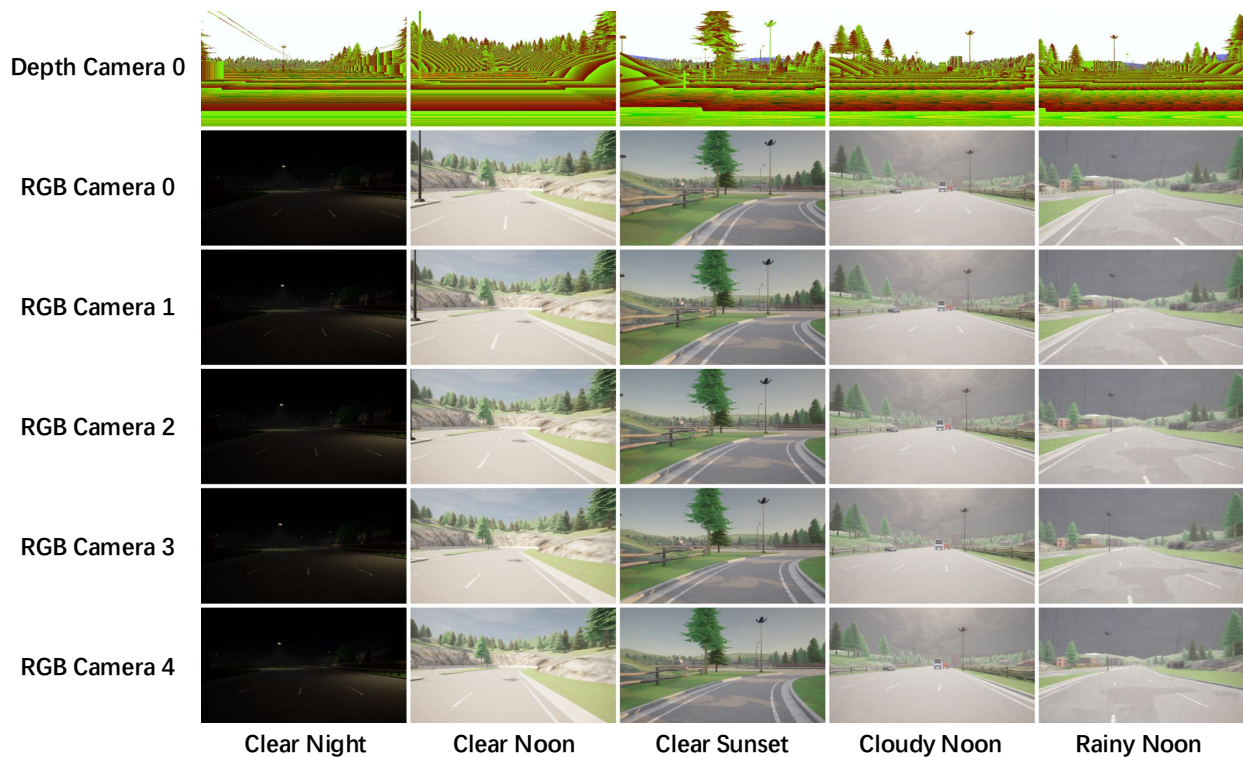


Figure 14. **Examples** of our synthetic data in **Town 06**.

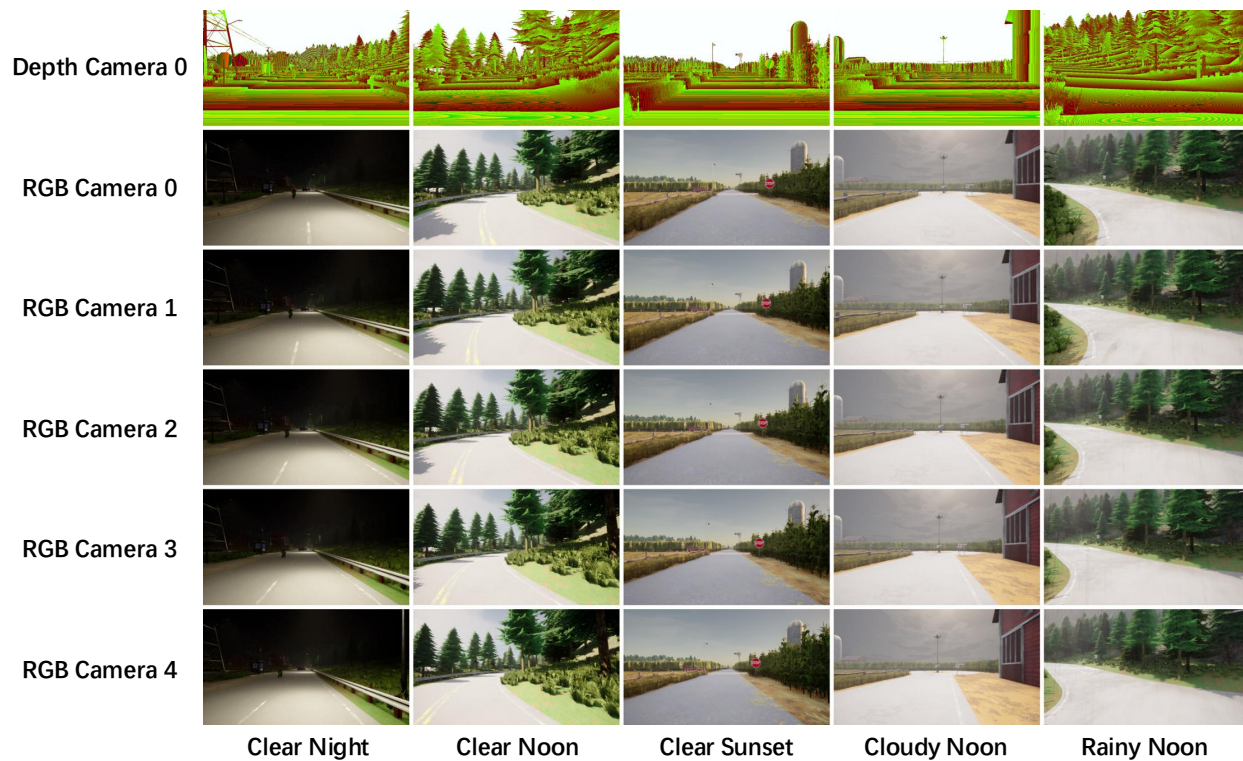


Figure 15. Examples of our synthetic data in **Town 07**.

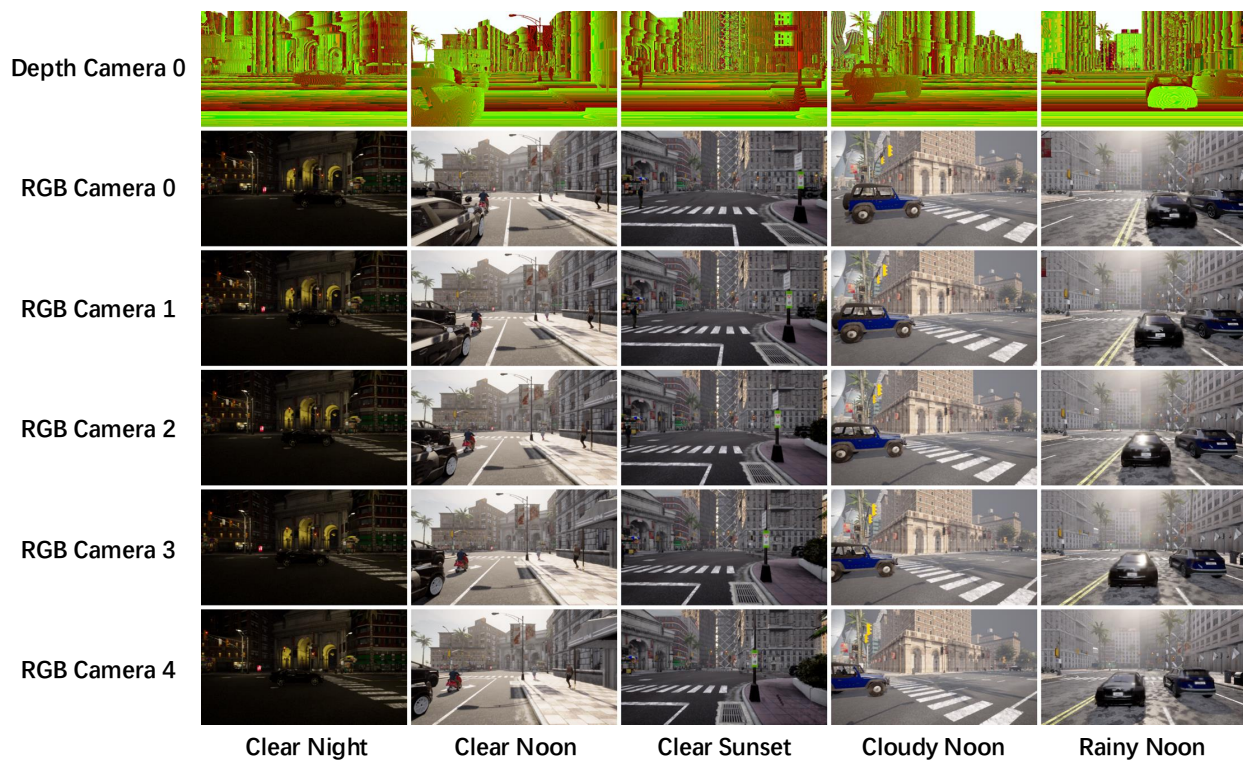


Figure 16. Examples of our synthetic data in **Town 10**.